JOURNAL OF GEOPHYSICAL RESEARCH: SPACE PHYSICS, VOL. 118, 6766–6776, doi:10.1002/jgra.50605, 2013

A comparison between resonant and nonresonant heating at EISCAT

C. J. Bryers,[1] M. J. Kosch,[1,2] A. Senior,[1] M. T. Rietveld,[3] and W. Singer[4]

Received 8 April 2013; revised 30 July 2013; accepted 30 September 2013; published 16 October 2013.

[1] We compare the height-integrated electron heating rates from O- and X-mode HF pump waves to extract the components due to resonant and nonresonant heating mechanisms in the ionosphere. We present results from a November 2011 campaign in Norway, using the European Incoherent Scatter (EISCAT) heater facility and UHF radar. We show that the theoretical nonresonant, ohmic heating due to the electromagnetic pump wave electric field agrees with observations for X-mode pumping. For O-mode pumping, the observed height-integrated heating rate exceeds the theoretical ohmic electron heating rate by a factor of 2–5, the excess being attributed to resonant heating mechanisms. In addition, a persistent UHF ion-line enhancement is observed for O-mode and, more unusually, X-mode pumping. We attribute the latter to O-mode leakage in the X-mode pulse. For O-mode, we see a descent in altitude of the ion-line enhancement and show that this is most likely due to ionization from pump-induced fluxes of suprathermal electrons. We estimate the ionization rate and determine an enhanced electron flux showing that approximately 10–20% of the pump power is transferred to high energy suprathermal electrons.

Citation: Bryers, C. J., M. J. Kosch, A. Senior, M. T. Rietveld, and W. Singer (2013), A comparison between resonant and nonresonant heating at EISCAT, *J. Geophys. Res. Space Physics*, *118*, 6766–6776, doi:10.1002/jgra.50605.

1. Introduction

[2] A powerful high frequency (HF) radio wave can induce perturbations in the ionosphere close to the reflection altitude. Upper hybrid resonance (UHR) is just one of several effects which can be stimulated when a right hand circularly polarized (in the northern hemisphere), O-mode wave propagates though the ionospheric plasma in the *F* region. The UHR altitude is where the pump wave frequency, f_0 is equal to the UHR frequency, f_{UH}:

$$f_{\mathrm{UH}} = (f_p^2 + f_e^2)^{1/2} = f_0 \tag{1}$$

where f_e is the electron gyrofrequency and f_p is the plasma frequency. The coupling of the pump electromagnetic wave to electrostatic, upper hybrid (UH) waves, which propagate perpendicular to the Earth's magnetic field lines, induces small-scale field-aligned striations, i.e., regions of reduced electron density. UH waves become trapped inside the striations resulting in saturation within a few seconds. This process of UHR can dramatically increase the ambient electron temperature above the background.

[3] A left hand circularly polarized, X-mode wave is unable to stimulate UHR in an overdense ionosphere since it is reflected back down before it reaches the UHR altitude [*Fejer*, 1979]. Instead, only nonresonant ohmic heating occurs. An O-mode wave also produces ohmic heating but not necessarily to the same degree as for an X-mode pump wave.

[4] As well as UHR, Langmuir turbulence can be stimulated parallel to the magnetic field line via the parametric decay instability (PDI) or the Oscillating Two Stream Instability (OTSI) [*Robinson*, 1989]. Langmuir waves are also thought to be responsible for electron acceleration. They are observed by the incoherent scatter radars at the so-called matching height where the electrostatic Langmuir waves have a wavelength which is half that of the radar. Langmuir waves can be created at many different altitudes but are only observed at the matching height of the radar which depends on its frequency. The radar detects pump-induced Langmuir turbulence as coherent backscatter, resulting in enhanced ion-line spectra, which may be misinterpreted as a high electron density and/or temperature. The Langmuir waves generated by the pump wave can also decay into ion acoustic waves and further Langmuir waves. Typically, these ion-line enhancements are observed during the first few seconds only (known as an ion-line overshoot) and die away after a few seconds once the pump-induced striations develop. Striations limit the pump power reaching the radar matching height by anomalous absorption [*Robinson*, 1989]. Occasionally, the enhancements persist throughout the pump on period which could be due to the presence of only weak striations (e.g., gyroharmonic pumping [*Ashrafi et al.*, 2006]) or due to a high enough power reaching the matching altitude despite anomalous absorption. When the electron temperature is below ∼1000 K, the PDI matching altitude for the European Incoherent Scatter (EISCAT) UHF radar

[1]Department of Physics, Lancaster University, Lancaster, UK.
[2]School of Physics, University of KwaZulu-Natal, Durban, South Africa.
[3]EISCAT Scientific Association, Ramfjordmoen, Norway.
[4]Leibniz-Institute of Atmospheric Physics, Rostock University, Kühlungsborn, Germany.

Corresponding author: C. J. Bryers, Department of Physics, Lancaster University, Lancaster, UK. (c.bryers@lancaster.ac.uk)

2169-9380/13/10.1002/jgra.50605

is above the UHR altitude [*Rietveld et al.*, 2000]. Since the background electron temperature is usually above 1000 K in the *F* region, the UHF matching height is normally found below the UHR height at EISCAT.

[5] In some cases, it is possible to observe an enhanced ion line which descends in altitude during the pump on period. *Djuth et al.* [1994] and *Ashrafi et al.* [2006] attributed ion-line descent to the increasing electron temperature which reduced the plasma recombination rate. This would increase the local electron density and cause the matching height to be found at a lower altitude. *Blagoveshchenskaya et al.* [2009] have reported pump-induced electron density enhancements of up to 25%. A density enhancement would cause the pump wave to reflect at a lower altitude and a descent of the enhanced ion-line backscatter would be observed. They determined that impact ionization was the most likely explanation for the density enhancements which is consistent with the findings of *Pedersen et al.* [2009] and *Pedersen et al.* [2011].

2. Methodology and Modeling

[6] During O-mode pumping, the increase in electron temperature is due to the combination of nonresonant ohmic heating by the electromagnetic pump wave and resonant ohmic heating from the electrostatic UH and Langmuir waves. For simplicity, these two mechanisms will be referred to as nonresonant and resonant heating respectively. We investigate how the two mechanisms affect the electron heating rates. In order to separate the two contributions, we modeled the electric field, E of the pump wave to estimate the height-integrated electron heating, $J_{\text{nonresonant}}$ due to the nonresonant heating mechanism alone. Determining the electric field of the pump wave allows an estimate of the heat source, $Q_{\text{nonresonant}}$ from the pump wave to be made:

$$Q_{\text{nonresonant}} = \frac{1}{2} Re[\mathbf{E}^* \cdot \overleftrightarrow{\sigma}_{\pm} \cdot \mathbf{E}] \tag{2}$$

where $\overleftrightarrow{\sigma}_{\pm}$ is the polarization dependent HF electric conductivity tensor for the contribution due to the electromagnetic wave only. The nonresonant height-integrated heating rate, $J_{\text{nonresonant}}$ is determined by integrating equation (2) in altitude. As an electromagnetic wave propagates through an overdense ionosphere, the electric field amplitude swells as the wave approaches reflection. This effect is to conserve Poynting flux as the group velocity of the wave decreases. This swelling also increases the heating of the electrons near reflection.

[7] To determine the absolute height-integrated heating rate, the use of the expression given by (2) would be satisfactory if no resonant mechanisms were stimulated, as is the case for X-mode pumping [*Gustavsson et al.*, 2010]. However, for O-mode pumping, plasma resonances cause additional heating. We require a second method to determine the total height integrated heating rate J_{total} which is independent of the heating mechanism. If the electric field model is good, for X-mode pumping, $J_{\text{nonresonant}} = J_{\text{total}}$. For O-mode pumping, $J_{\text{nonresonant}} \neq J_{\text{total}}$ since additional heating occurs from the electric field of the induced electrostatic waves. Determining J_{total} and $J_{\text{nonresonant}}$ independently enables us to infer quantitatively the electron heating due to the plasma resonances for O-mode heating. We note also that the electric field model used assumes no anomalous absorption from striations. This means therefore that $J_{\text{nonresonant}}$ is an upper bound.

2.1. Heat Source Model; $\mathbf{J_{total}}$

[8] As the HF pump is turned on, the *F* region electrons begin to increase in temperature due to the presence of the pump wave. The temperature increase is a balance between the heat source supplied by the pump and the two local energy loss mechanisms; the electron cooling rate and field-aligned heat conduction. We solve the electron energy equation to determine the heat source needed to produce the observed electron temperature profile as measured by the EISCAT UHF incoherent scatter radar. Since the radar analysis assumes a Maxwellian electron flux, J_{total} is the total energy transferred to the Maxwellian electrons by the pump. The method is briefly outlined below but a full description can be found in *Bryers et al.* [2012]. The electron energy equation is described by *Schunk and Nagy* [1978]:

$$\sin^2 I \frac{\partial}{\partial z}\left(K^e \frac{\partial T_e}{\partial z}\right) + \sum Q_e + \sum L_e = 0 \tag{3}$$

where I is the angle of inclination of the Earth's magnetic field (77.5° for EISCAT). The heat source term is $Q_e = Q_{\text{total}} + Q_{\text{photo}}$, where Q_{total} and Q_{photo} are the heat sources from the HF pump and the solar photoionization respectively. T_e is the electron temperature. L_e is the sum of the electron energy cooling rates. These were taken from *Campbell et al.* [2004] for the vibrational excitation of N_2 and *Pavlov* [1998a] for the rotational excitation of N_2. The vibrational and rotational excitations of O_2 were taken from *Jones et al.* [2003] and *Pavlov* [1998b], respectively. Both the cooling due to the excitation of the $O(^1D)$ and elastic collisions with ions were taken from *Schunk and Nagy* [1978, equations 34 and 37, respectively]. The thermal conductivity K^e is given by *Banks* [1966]. We solve equation (3) for the thermal steady state case which is achieved toward the end of the pump-on period.

[9] The heater contribution of the heat source, Q_{total} was approximated by a Gaussian form:

$$Q_{\text{total}} = \frac{1}{w\sqrt{2\pi}} J_{\text{total}} \exp\left(\frac{-(z-z_0)^2}{2w^2}\right) \tag{4}$$

where J_{total}, z_0, and w are constants to be determined. The values of J_{total}, z_0, and w give the height-integrated heating rate in W/m^2, the height at which most of the pump wave energy is deposited and the half-width of the Gaussian heat source, respectively. Solar photoionization is of the same form and can be determined during a pump-off period.

[10] J_{total}, z_0, and w were varied and equation (3) was solved for T_e until the difference between the modeled T_e and the measured T_e from radar observations was minimized.

2.2. Electric Field Model; $\mathbf{J_{nonresonant}}$

[11] To estimate the electric field amplitude of the pump wave, we use the model of *Shoucri et al.* [1984]. It calculates the swelling of the electric field as the wave approaches HF reflection in an overdense ionosphere where electron heating is dominant. We refer the reader to their manuscript for a full description. One thing to note is that their model, for simplicity, assumed vertical propagation of the electromagnetic

wave and a vertical magnetic field. In reality this does not exist at any of the heating facilities around the world. When using their model *Shoucri et al.* [1984] assume that a small angle between the heater direction and the magnetic field does not have a great effect on the electric field calculation.

[12] To test this, we modified the model slightly for use with 12° off-vertical heating (field-aligned at EISCAT). When pumping off-vertical, the center of the pump wave beam may not reach the altitude where the plasma frequency equals the pump wave frequency, but could refract downward before it can do so. The Spitze angle is ∼6° at EISCAT which is the greatest zenith angle for which the pump wave reaches the highest possible reflection height. Not reaching the true reflection height could limit the electric field swelling and result in the model overestimating the ohmic heating. Instead we calculate $Q_{\text{nonresonant}}$ up to the refraction height found by the use of the *Jones and Stephenson* [1975] ray tracing model. This is typically 1–4 km below the nominal HF reflection height. This refraction height is the maximum altitude reached by the center of the pump beam. The ray trace model also calculates the refractive index of the wave as it propagates. For completeness we use the ray trace refractive index and refraction height in the electric field model of *Shoucri et al.* [1984]. We conclude that the difference between $J_{\text{nonresonant}}$ using modified and the original version of the electric field model was small (<10%) and is within the experimental uncertainties.

[13] It is important to note that the two models used here to calculate the height-integrated heating rates are very different. The electric field model is a forward model and uses the heater power to predict how the electromagnetic wave would behave as it propagates through the ionosphere. The heat source model, used to find J_{total}, is an inverse model using the measured electron temperatures to determine the heat source.

2.3. D Region Absorption

[14] To calculate the electric field, the free space electric field must be reduced due to the absorption of the HF pump wave as it propagates through the *D* region. We use the model of *Senior et al.* [2010] to estimate the self absorption of the electromagnetic wave as it increases the local plasma temperature and hence modifies the electron-neutral collision frequencies. The model accounts for the polarization and frequency of the wave. A full description of the *D* region absorption model can be found in *Senior et al.* [2010]. We use the model for the equilibrium case which assumes electron temperatures have reached a constant level and will remain unchanged for as long as the heater remains on. An averaged background electron density profile was used from before and after each pump-on period as input to the model.

[15] We found that at low altitudes the EISCAT UHF radar electron density data was low and often negative where the power received was close to the background noise. This can occur when the radar wavelength is comparable to the electron Debye length causing the density to be underestimated. To correct this, data from a second radar (discussed in section 3) was used for low altitudes up until both densities agreed (approximately 75 km). This density profile was used to determine the *D* region absorption.

2.4. High-Energy Electron Flux

[16] Since J_{total} shows how much of the heater power is transferred to the electrons in the Maxwellian thermal energy distribution, observation of a descending ion-line enhancement due to ionization during O-mode pumping allows us to make an estimate of the high-energy, non-Maxwellian electron flux. We can estimate the ionization rate and use this to determine the high-energy suprathermal electron flux. Considering the electron energy loss processes, an estimate of the energy transferred by the pump to high-energy electrons can be made.

[17] A descent in the ion-line enhancement during pumping is due to a local electron density increase in the vicinity of the pump wave reflection height. *Blagoveshchenskaya et al.* [2009] tested three different mechanisms which could cause this density increase: (1) Reduced temperature dependent recombination rates. (2) Redistribution of the electron density due to diffusion. (3) Ionization of the neutral species by pump accelerated electrons.

[18] To test whether the electron temperature enhancement is large enough to explain the decrease in altitude of the enhanced ion-line due to reduced recombination we follow the same process of *Blagoveshchenskaya et al.* [2009]. The electron density change due to changing plasma temperature is given by *Schunk and Nagy* [2000]:

$$\frac{\mathrm{d}n_e}{\mathrm{d}t} = q(z,t) - \frac{(k1[N_2] + k2[O_2])}{1 + \frac{k1[N_2]}{a1 \times n_e} + \frac{k2[O_2]}{a2 \times n_e}} \times n_e \tag{5}$$

where n_e is the electron density, q is the altitude and time dependent production rate due to the pump and photoionization, and $[N_2]$ and $[O_2]$ are the concentrations of nitrogen and oxygen respectively. $k1, k2, a1$, and $a2$ are the temperature-dependent rate coefficients taken from *Richards* [2011]:

$$k1 = 1.2 \times 10^{-18} \times (300/T_i)^{0.45},$$
$$k2 = 9 \times 10^{-19} \times (T_i/900)^{0.92},$$
$$a1 = 4 \times 10^{-13} \times (300/T_e)^{0.85},$$
$$a2 = 1.95 \times 10^{-13} \times (300/T_e)^{0.7}.$$

[19] The above expressions are valid for the temperatures measured during this particular experiment, and different equations may be used if T_i or T_e are above or below a certain temperature threshold. See *Richards* [2011] for a more extensive list. Solving equation (5) for n_e during pump on, assuming steady state and assuming q is only due to photoionization (determined during pump off) gives the electron density enhancement due to reduced recombination only.

[20] *Blagoveshchenskaya et al.* [2009], citing the work of *Meltz and LeLevier* [1970], show that the density enhancements are unable to be explained by diffusion along the field line since the expansion of the plasma has a response time of 5–10 min and is too slow to allow such a density enhancement to occur in a 2 min heater-on cycle. We calculate the field-aligned ambipolar diffusion:

$$D = \frac{k_B T}{m_i \nu_{in}} \tag{6}$$

where D is the ambipolar diffusion coefficient, $T = T_e + T_i$, m_i is the ion mass and ν_{in} is the ion-neutral collision frequency.

The change of electron density with respect to time is:

$$\frac{\mathrm{d}n_e}{\mathrm{d}t} = \frac{\partial}{\partial z}\left(D\frac{\partial n_e}{\partial z}\right) \tag{7}$$

[21] If the reduced recombination and diffusion rates are small, the action of the pump wave must be causing ionization. The ionization rate due to the pump, needed to cause the observed density enhancements can be found using equation (5). For ionization to occur from the pump wave, the electrons in the plasma must be accelerated to high enough energies so that collisions with neutral species cause them to lose an electron. *Pedersen et al.* [2009] determined the energy required by the pump to enable this, assuming each electron loses 20 eV per ionization. They assumed a 20 km wide layer in which the electrons lose their energy and found that approximately 10% of the total heater power is required to observe this level of ionization. They did not calculate the *D* region absorption so their estimate would be greater if absorption levels were significant. Rather than assuming 20 eV is lost per electron, we can take a more rigorous approach by considering the ionization cross sections.

[22] Since the HF pump wave is able to accelerate electrons to the energies required for ionization, we can estimate the non-Maxwellian, high energy flux of electrons using the ionization rate, *q*. *Gustavsson et al.* [2006] and *Gustavsson and Eliasson* [2008] were able to estimate the electron flux by using multiwavelength (630.0, 557.7, 844.6, and 427.8 nm) optical observations. To do this they minimized the difference between the measured and modeled optical intensities until they had an energy and altitude dependent electron flux. In the experiment reported here we were unable to observe optical signatures since it was daylight, but based on the findings of *Gustavsson and Eliasson* [2008] we are able to constrain the energy distribution form. Their main findings were the following: (1) The acceleration of the electrons occurs close to the UHR height. (2) The flux distribution plateaued between 3.5 and 10 eV. (3) There was a high-energy tail from 10 eV upward. We approximate this high-energy tail to be power law like following numerical simulations by *Wang et al.* [1997].

[23] The energy dependent flux $f(E)$ and q are related by

$$q = \sum_i \int_{E_{\mathrm{th},i}}^{\infty} n_i f(E)\sigma_i \mathrm{d}E \tag{8}$$

where i refers to the species being ionized, n is the density of the neutral species, $E_{\mathrm{th},i}$ is the threshold energy of ionization and σ is the ionization cross section. We impose that at 3.5 eV, the Maxwellian and the high-energy electron fluxes become equal where the plateau begins and from 10 eV upward the flux follows the power law given by:

$$f(E) = AE^{-B} \tag{9}$$

where A is found easily since we know the Maxwellian flux at 3.5 eV from the UHF radar data. We calculate the Maxwellian flux using the UHF radar data, solve equation (8) for q using an initial guess of B in equation (9) and minimize the difference between the observed and modeled q until $f(E)$ is determined.

[24] In thermal equilibrium the energy lost by an electron equals the energy gained by an electron from the pump wave. The energy loss E_{loss} in Wm^{-2} for a specific process is given by:

$$E_{\mathrm{loss},j} = x \cdot E_{\mathrm{th},j} \cdot \sum_i \int_{E_{\mathrm{th},j}}^{\infty} n_i f(E)\sigma_j \mathrm{d}E \tag{10}$$

where x is the width of the layer in which the electrons lose their energy and $E_{\mathrm{th},}$, σ_j are the threshold energies and cross sections respectively, associated with the various loss processes, j.

[25] Once $f(E)$ is known we can estimate the optical emission intensities of the artificial aurorae. The red (630.0 nm) and green (557.7 nm) line emissions are given by *Gustavsson and Eliasson* [2008]:

$$I_{6300} = 10^{-10}A_{6300}\int_{E_{\mathrm{th}}}^{\infty}\tau[I_{5577}(z) + n_O\int_0^{\infty}\sigma(E)f(E)\,\mathrm{d}E]\mathrm{d}z \tag{11}$$

$$I_{5577} = 10^{-10}A_{5577}\int_{E_{\mathrm{th}}}^{\infty} n_O\int_0^{\infty}\sigma(E)f(E)\,\mathrm{d}E\mathrm{d}z \tag{12}$$

where σ is the cross section associated with each emission, n_O is the density of oxygen, z is altitude, τ is the altitude varying $\mathrm{O}(^1\mathrm{D})$ lifetime, $A_{6300} = 5.15\times10^{-3}\ \mathrm{s}^{-1}$ is the Einstein coefficient for the transition from $\mathrm{O}(^1\mathrm{D})$ to the $\mathrm{O}(^3P_2)$ ground state, and A_{5577}=0.941. The cross sections used are taken from *Itikawa et al.* [1986, 1989], and *Itikawa and Ichimura* [1990] and are the same as those shown in *Gustavsson and Eliasson* [2008, Figure 3].

3. Experiment

[26] To quantify the resonant and nonresonant plasma heating components we performed an experiment on 15 November 2011 at the European Incoherent Scatter Scientific Association (EISCAT) heating facility [*Rietveld et al.*, 1993]. The heater was operated in daylight from 10 to 14 UT in a 2 min on, 2 minute off-pump cycle, alternating between O-mode and X-mode in subsequent heater-on periods. The EISCAT UHF (930 MHz) incoherent scatter radar [*Rishbeth and van Eyken*, 1993], near Tromsø, northern Norway (69.58°N, 19.21°E) observed the ionospheric electron density, N_e and electron and ion temperatures, T_e and T_i, respectively. Both the heater and the UHF radar were field-aligned (12°S). The radar code used was Beata, which enabled measurements from 50 to 700 km in altitude with a minimum of 5 s resolution and an unambiguous range resolution of 3.5 km. We analyze the radar data with 7 km, 60 s resolution to reduce measurement error. Measurements from the MF partial reflection radar [*Singer et al.*, 2008] at Saura, Andøya (69.3°N, 16.0°E) (130 km WSW of EISCAT) were used to determine the lower *D* region electron density profile where the UHF radar underestimated the electron density.

[27] The effective radiated power (ERP) of the O- and X-mode pump waves were 727 MW and 874 MW, and their frequencies were 7.273 MHz and 7.953 MHz, respectively. The frequencies were chosen so that the nominal HF reflection height of the pump waves were the same for both polarizations since the X-mode reflects at a half electron gyrofrequency (∼680 kHz) below the O-mode. The heater antenna gain is frequency-dependent, accounting for the different ERP's.

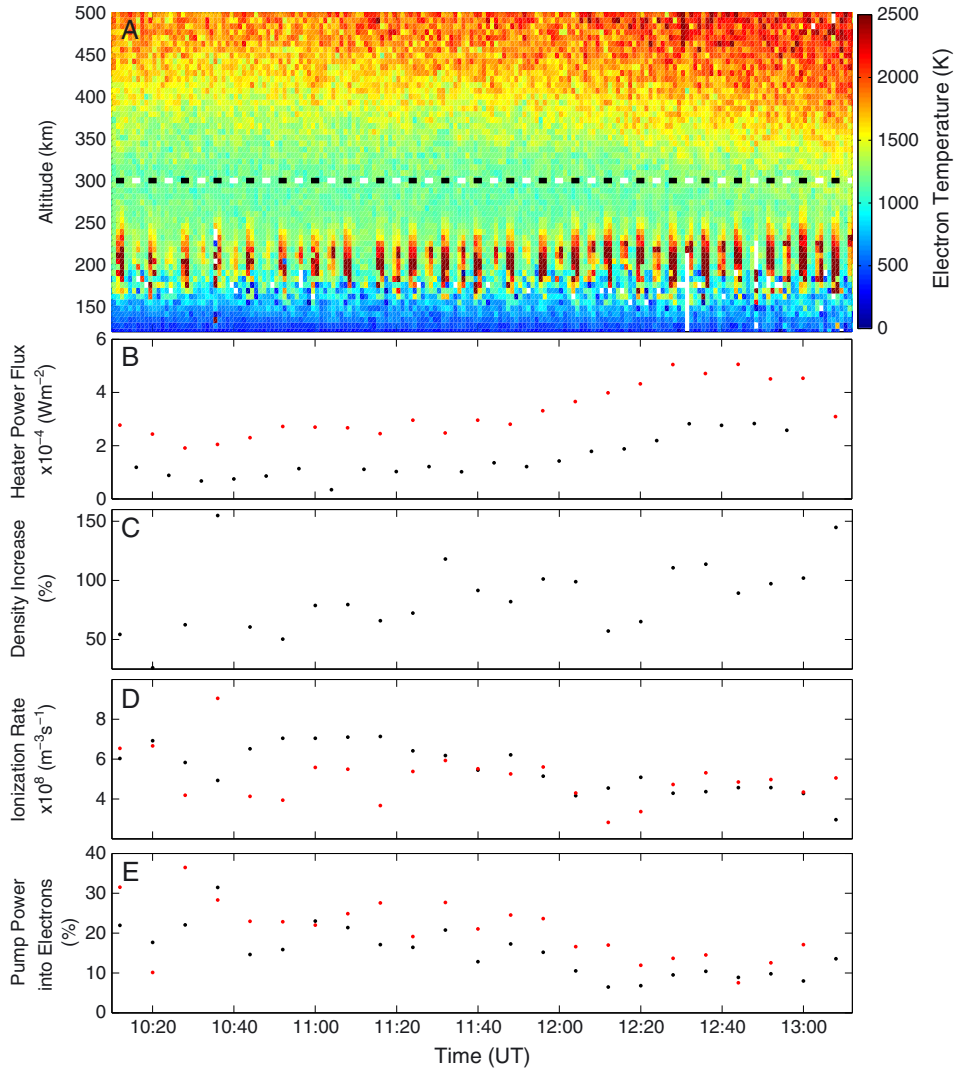

Figure 1. (a) The electron temperature profile from 10 to 13:20 UT on 15 November 2011 as measured by the EISCAT UHF radar. The altitude resolution was 7 km and the time resolution was 60 s. The pump polarization is shown plotted as black or white dashes for O- and X-modes, respectively. (b) The modeled heater power flux for O-mode (red) and X-mode (black) at reflection altitude. (c) The percentage increase of the electron density during pump on close to the reflection height. (d) The modeled photoionization and pump ionization rates (black and red, respectively). (e) The percentage pump power transferred to the low-/high-energy electrons in red/black for O-mode heating.

4. Results and Analysis

[28] Figure 1a shows the UHF radar electron temperature profile with a temporal resolution of 60 s and range resolution of 7 km. The black/white dashes show where the pump was transmitting in O-mode/X-mode. The temperature enhancement as the heater is switched on is clear. The temperature was higher for the O-mode case, even though on the ground this polarization had less power than the X-mode. f_oF2 was around 11 MHz at 10 UT so the ionosphere was overdense. The ionosphere went underdense at around 13:10 UT. We only examine the overdense cases here to ensure that resonances still occur since UHR ceases when the ionosphere goes underdense. Underdense heating was confirmed to occur at 13:10 UT by ray tracing analysis using the measured electron density profiles. This is consistent with the increased altitude extent of the temperature enhancements as the wave reflection height is increased and the electron cooling rates are reduced.

[29] Figure 2 shows the median rise and fall of the electron temperature during heater on and the subsequent 120 s after heater off from 23 pump cycles. The red points show the temperature for the O-mode pulses, and the black shows the X-mode pulses. The temperature recordings were taken from 5 s integrated UHF radar data at 8 km above the ion-line enhancement height (discussed below). This is because temperatures in the ion-line enhancement range gates can be erroneous due to a breakdown of the radar analysis assumptions. At this altitude the heater enhances the natural ion-acoustic waves, and the radar analysis incorrectly interprets these as temperature enhancements. This means that for the range gate where this occurs, the derived temperatures cannot be assumed to be accurate. The blue dashed line indicates the time when the heater was switched off. The

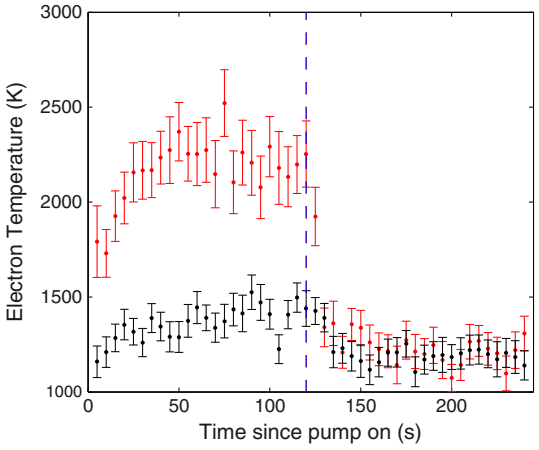

Figure 2. The epoch median electron temperature time development. Red and black refers to O- and X-mode enhancements respectively. The blue dashed line indicates the time when the heater was switched off.

temperature enhancement above background for O-mode pumping was on average 1400 K compared to 400 K for X-mode. The background temperature was approximately 1100 K. We observe that the O-mode enhancement has a rapid onset compared to the X-mode. In the first 5 s, the O-mode enhancement has reached 600 K above background and typically peaks at 50 s. For the X-mode pulses there is a much slower rise, and the peak enhancement is reached closer to 70 s after pump on.

[30] We observe a descending ion-line in the UHF radar data when pumping with O-mode. If the electric field of the pump wave exceeds the PDI or OTSI threshold, an enhanced ion-line is observed. The PDI signature manifests itself as enhanced shoulders on the usual double peak ion-line spectra and OTSI appears as an enhanced peak in radar spectra at the zero doppler shift position [*Robinson*, 1988]. This causes the analysis software to misinterpret the spectra as high electron densities and temperatures in the enhanced ion-line range gates and must be ignored. This becomes important when determining the heat source, J_{total}, from the electron temperature profiles.

[31] Figure 3 shows how these backscatter enhancements appear in the UHF radar plasma density data. The false high-density regions, shown in black and dark red can be seen around 200–220 km. We observed an ion-line enhancement for both O- and X-mode pumping. For the O-mode pulses it descends in altitude throughout the 2 min heater on cycle which we attribute to a descent in the reflection altitude of the pump wave. This altitude decrease is typically 10–15 km throughout the experiment. We will discuss this further in section 4.2 along with an explanation for the appearance of the nondescending enhancement during X-mode pumping.

4.1. Height-Integrated Heating Rates

[32] Figure 4 shows a typical plot of the estimated electron temperature profile in red, compared to the measured UHF temperatures for an O-mode (Figure 4, left) and X-mode (Figure 4, middle) case close in time, following the method described in section 2.1. The O-mode case here was for the heater pulse beginning at 10:28 UT and the X-mode pulse began at 10:24 UT. We inspect this particular profile since the ion-line height remains in the same range gate throughout the heater on pulse, and we observe only a small descent unlike those found for the other pulses. This allows us to compare the heights of the fitted heat source more fairly without the added complication of the descending ion line.

[33] Figure 4 (right) shows the Gaussian heat source profile, Q_{total} for the O-mode in red and for the X-mode in black. The heat sources' half widths, w, are both narrow in altitude extent (±5 km of the Gaussian peak) as was found by *Bryers et al.* [2012]. The height, z_0 of the heat source for the O-mode case is below that of the X-mode case. The X-mode heat source height was found at 219 km and the O-mode case was at 208 km. For this particular case, the HF reflection altitude was 220 km and the UHR height was 3 km below this. *Bryers et al.* [2012] showed that for O-mode polarization, the height of the heat source was found to be close to the UHR height where the majority of the heating occurs. In the case of the X-mode polarization, the majority of heating is due to the swelling of the pump wave electric field as it approaches reflection. We can therefore expect that there will be a separation in the heat source altitudes for the different polarizations. We find that the heat source for the O-mode case is below the pump wave reflection height, and for the X-mode pulse, it is close to the reflection height as expected. The difference between the UHR height and the O-mode heat source height is possibly due to the altitude extent of the striations (∼20 km) [*Senior et al.*, 2004] and [*Graham and Fejer*, 1976]. Anomalous absorption of the pump wave in the lower part of the striations, below the UHR height, would diminish the pump wave energy reaching the true reflection height. From this one case with a small ion-line descent, we find that the result agrees with our theory.

[34] We note the high variation in temperatures between range gates in the profiles below 200 km which are accompanied by a larger error than those found at other altitudes. In the region below 200 km, before the electron density increases toward the F region peak, the radar signal-to-noise ratio may be lower and the associated temperature measurements become noisy. The fitting process used here places less weight on measurements with a higher error to counteract this effect.

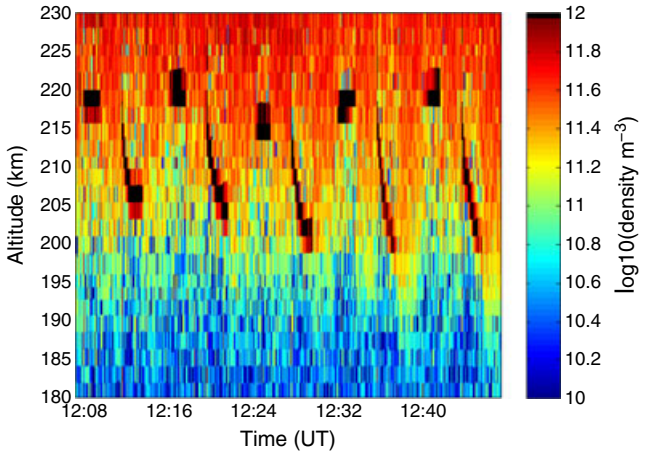

Figure 3. Temporal evolution of the pump-induced UHF ion-line enhancement. The descending ion-lines occur during O-mode pumping.

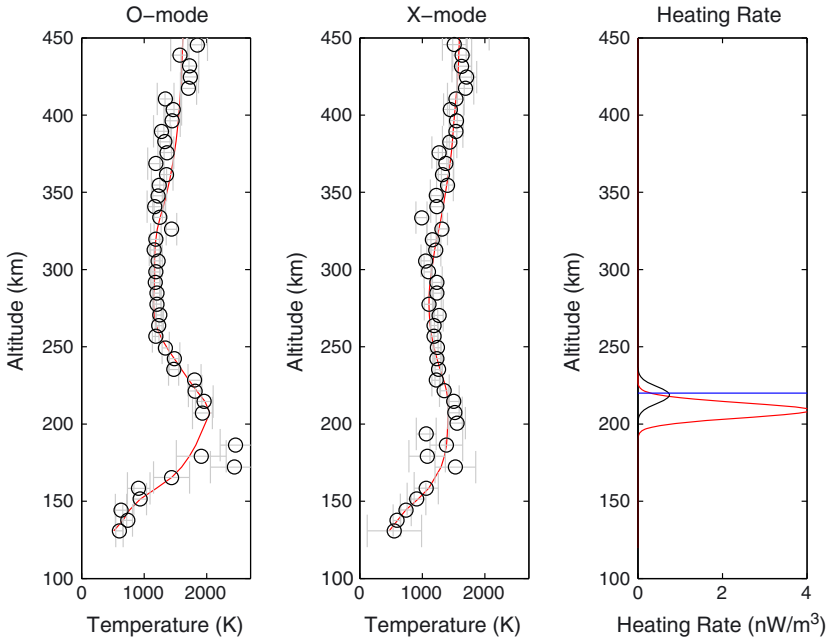

Figure 4. A typical output from the heat source fitting model. (left) The measured UHF radar electron temperature profile for an O-mode pulse; the red line shows the modeled temperature. (middle) Same as in Figure 4 (left), but for an X-mode pulse. (right) The two Gaussian heat source profiles for an O-mode (red) and X-mode (black) case. Integrating these in altitude gives J_{total}. The blue line shows the HF reflection height at 220 km.

[35] In Figure 5, top, the height-integrated heating rate, J, is plotted in time. The red dots show J_{total} for the O-mode and the black dots for the X-mode pump pulses. The crosses of the same color show the $J_{\text{nonresonant}}$ estimated using the electric field model and integrating equation (2) in altitude. The figure shows that $J_{\text{nonresonant}}$ for the O-mode pump pulses are similar to that of the X-mode even though there is more energy available in the O-mode heater beam. This is purely a coincidence for this data set given the ERP's used and is due to the nature of the D region absorption; i.e., greater loss for X-mode than O-mode. Figure 1b shows the heater power flux at the reflection height for O-mode/X-mode in red/black, ignoring anomalous absorption. It is possible to see an increase in $J_{\text{nonresonant}}$ throughout the experiment as the heater self absorption in the D region decreases over time from 7 to 3 dB.

[36] We find that $J_{\text{nonresonant}}$ agrees well with J_{total} for the X-mode pumping with typical errors being $\pm 2\times10^{-6}$ Wm^{-2} for both models. These error estimates are calculated by randomly varying the electron density and temperature profiles within the error bounds of the measurements at each altitude. In Figure 5, bottom, J is plotted for X-mode pumping with the electric field model estimate on the x axis and heat source estimate on the y axis. The dotted red line shows where $J_{\text{total}} = J_{\text{nonresonant}}$. The agreement between the two models shows that the electric field model is good. This gives us confidence that the electric field model can be applied to the field-aligned case (12° S at EISCAT). The validity of the model for a field-aligned O-mode pump wave in the absence of UHR (gyroharmonic pumping) was tested and found to be good also (see Appendix A).

[37] For the O-mode case in Figure 5, we see that J_{total} is significantly larger than $J_{\text{nonresonant}}$. The difference between the two can be attributed to the additional heating from resonant mechanisms. We find that the resonant heating is approximately 2–5 times greater than the nonresonant heating and is relatively constant throughout the experiment.

[38] The efficiency of transferring the pump wave energy to the Maxwellian thermal electrons is calculated by J_{total}/S where S is the heater power flux shown in Figure 1b.

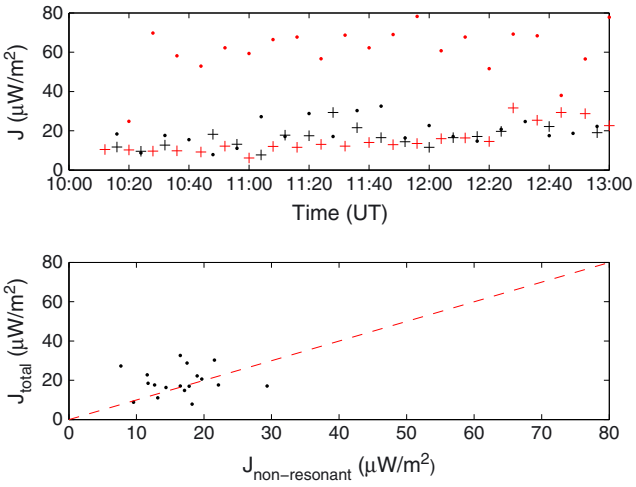

Figure 5. (top) The height-integrated heat sources from the electric field model, $J_{\text{nonresonant}}$ (crosses) and the height-integrated heat source estimate from the temperature fitting method, J_{total} (dots). Red/black refers to the O-mode/X-mode respectively. (bottom) The X-mode total height-integrated heating rate plotted against the modeled nonresonant component. The dashed line shows $J_{\text{total}} = J_{\text{nonresonant}}$.

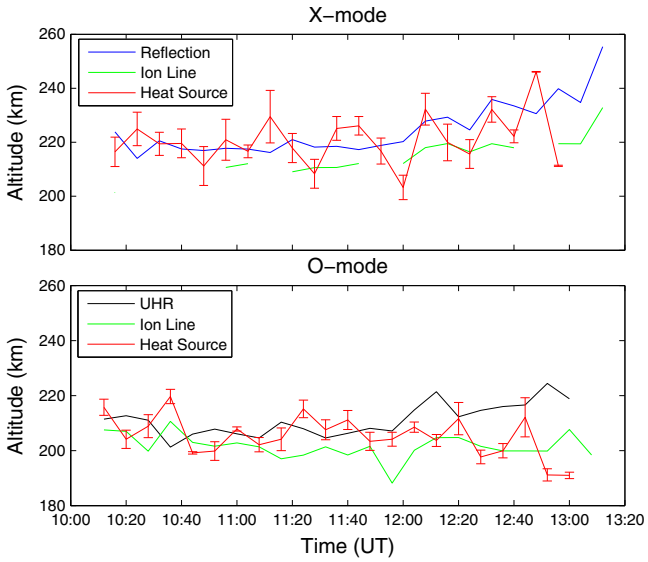

Figure 6. (top) The reflection height for the X-mode and O-mode pump wave (blue), the UHF ion-line enhancement height (green), and the estimated height of the heat source (red). (bottom) The UHR height (black) for the O-mode pump wave including the descent of the reflection height, the UHF ion-line enhancement height at the end of pump on (green), and the estimated height of the heat source (red).

For O-mode this is found to be around 35% at the start of the experiment falling to around 15% toward the end. These are shown in red, plotted in Figure 1e. The X-mode efficiency (not shown) is lower at 20% to begin with falling to 10%. *Bryers et al.* [2012] found the O-mode heating efficiency to be around 60–70% for high pump powers (565 MW ERP). The results presented here show a lower efficiency for high-power O-mode; however, in this experiment we use a higher frequency (7.273 MHz compared to 6.2 MHz in *Bryers et al.* [2012]), a higher power (727 MW compared to 565 MW), and we observe a lower *D* region absorption (7–3 dB compared to 12–9 dB). These effects combined may alter how efficient the heating process may be. *Hansen et al.* [1992] found the O-mode heating efficiency at Arecibo to be around 20% which is consistent with our observations. In section 4.3 we discuss another possible explanation as to why the efficiency could be lower.

[39] Figure 6, top shows the altitudes, z_0, of the fitted heat sources for the X-mode and for O-mode in Figure 6, bottom, in red. The blue line shows the reflection height of the pump wave in Figure 6, top, and the UHR altitude is shown in black in Figure 6, bottom. These were calculated using the electron density profiles prior to the heater being switched on. We reduced the UHR height by the same distance as for the enhanced ion-line descent during O-mode pump on. The green lines show the height of the enhanced ion-line for the steady state which were typically 10 km below the reflection height.

[40] The height of the heat source for the X-mode agrees with the reflection height for the majority of the experiment, but there are some cases where it is found slightly below. The height of the O-mode heat source is below that of the X-mode for most cases. Taking into consideration the decrease in altitude of the O-mode reflection height during the heater on period, we find that the heat source altitude remains close to the steady state UHR height for most of the pulses.

[41] The important thing to note is that the heat sources of the X-mode pulses are found close to the reflection height in most cases where electric field swelling maximizes. In the case of the O-mode pulses, much of the energy is deposited into the electrons via the UHR mechanism before the pump wave electric field is able to swell to large amplitudes as it approaches reflection. Striations have the effect of reducing the available pump wave energy to heat electrons via the nonresonant mechanism because of UHR and its related anomalous absorption [*Robinson*, 1989]. It is for this reason that the electric field model estimates a maximum ohmic heating rate for O-mode pumping. The altitude extent of the striations (typically ∼20 km [*Senior et al.*, 2004]) mean that the pump wave energy could be absorbed over a wide range of altitudes around the UHR height.

4.2. Ion-Line Descent

[42] By investigating the descending ion-line enhancements, we can make an estimate of the high energy electron flux following the process discussed in section 2.4.

[43] To estimate the electron density enhancement needed to reduce the ion-line altitude, we found the electron density at the starting ion-line height before the heater is turned on and compare to the density at the lower steady state height. Figure 1c shows the electron density enhancement as a percentage during the experiment. We find that the average density enhancement is approximately 80%. The percentage increases slowly as the heater power flux increases and the background electron density decreases.

[44] First, we determine if the enhanced electron temperature is great enough to explain this density increase by reducing the recombination rate of the plasma. Using equation (5), we find that the observed enhanced plasma temperature during pumping is only able to account for, on average, 2.5% of the density increase. We can conclude that the majority of the density enhancement cannot be due to reduced recombination.

[45] Using equation (7), we estimate the change in electron density due to diffusion along the field line. We find that during pump on, the diffusion causes the electron density change to be an order of magnitude smaller than the source and loss terms in equation (5) and is therefore negligible. We conclude that the descending ion-line enhancements are due to ionization from the pump wave as did *Blagoveshchenskaya et al.* [2009].

[46] Using equation (5) we estimate the production rate, q, needed to overcome the recombination rate in order to achieve the density enhancements observed. Figure 1d shows the photoionization rates during pump off in black and the pump-induced ionization rates in red. They are lower than those observed by *Pedersen et al.* [2009] who saw a much greater enhancement in electron density. For the majority of cases, the photoionization rate is higher than that due to the pump.

[47] Since we know the ionization rate due to the pump, we can solve equations (8) and (9) to determine the energy dependent electron flux $f(E)$ by using the ionization cross sections. Minimizing the difference between the measured and modeled q gives the electron flux and a value of B in

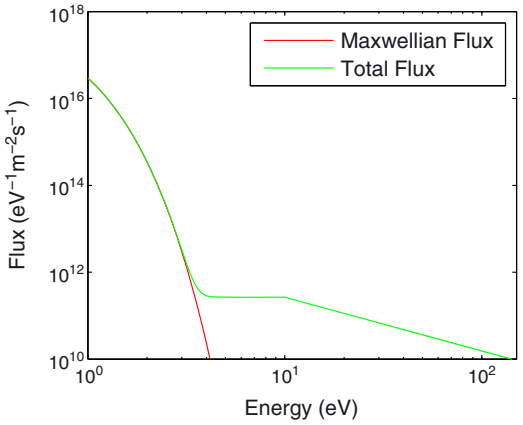

Figure 7. A typical estimate of the enhanced flux of electrons during HF O-mode heating at the UHR height.

equation (9). The result of a typical flux estimate is shown in Figure 7.

[48] We find that B is 1–2 for most cases. From *Gustavsson and Eliasson* [2008, Figure 10], we deduce that $B \sim 2$, which is in agreement with our results. We determine the total energy transferred by the pump wave to the non-Maxwellian suprathermal electrons assuming a 20 km wide layer, like *Pedersen et al.* [2009], by using equation (10). Considering all of the loss processes, we find that in total 10–20% of the heater, energy is transferred to the electrons with energy exceeding 3.5 eV, approximately half of which is lost during ionization.

[49] Using equations (11) and (12) gives estimates for I_{6300} between 30 and 80 R and for I_{5577} between 10 and 30 R. These estimates are in good agreement with previous experiments performed at EISCAT [e.g., *Kosch et al.*, 2007] giving confidence in our analysis. Without direct observations of the optical emissions, something that is controlled by weather conditions, time of day, the state of the ionosphere, and technical limitations, it is difficult to accurately determine $f(E)$. We have shown that an estimate can be made using the ionization rate alone, which gives sensible results based on previous findings.

4.3. Ion-Line Enhancement Strength and the Effects of Striations

[50] Figure 8 shows the 5 s integrated spectra for the X-mode in black, the O-mode in red at the ion-line enhancement altitude, and a typical heater off spectrum in blue at a time close to the end of the experiment. The power is in arbitrary units. For the O-mode case, both OTSI and PDI are stimulated, and the central peak is higher than the two peaks either side indicating that OTSI dominates. For the X-mode spectrum, the central peak is lower than the two peaks either side, and the power is greater for all three peaks.

[51] Usually, the PDI and OTSI signatures are not observed for the X-mode case because the pump wave reflects before it can reach the matching height for PDI/OTSI. However, there is evidence that this is not true in both Figures 3 and 8. Figure 3 shows the enhanced ion-lines in the X-mode pulses at a slightly higher altitude than for the starting O-mode height. This would indicate that the heater frequency causing this instability was of a higher frequency than for the O-mode waves (7.273 MHz), and we deduce that there was O-mode leakage within the X-mode pulse (7.953 MHz). During pumping, it is difficult to achieve a 100% pure polarization so even though a 874 MW ERP X-mode beam is being transmitted, a small percentage would be O-mode with the same frequency (i.e., 7.953 MHz). We find the plasma frequency gradient from the radar data close to the matching heights to be approximately 0.12 kHz m^{-1}. We observe the difference in ion-line altitude for the O- and X-mode pulses to be 5.5 km and conclude that the difference in plasma frequency between the two altitudes is 663 kHz. This is close to the expected difference of 680 kHz of the two heater frequencies.

[52] Using the electric field model, we estimate that the O-mode leakage ERP is ∼10 MW, enough to ensure that the electric field of the pump wave is above the threshold of PDI and OTSI at the radar matching height [*Robinson*, 1989]. *Stubbe et al.* [1992] found that Langmuir turbulence could be observed by the EISCAT UHF radar with an O-mode pump wave with an ERP above 17–35 MW. We note that the ERP's quoted by *Stubbe et al.* [1992] were 21–43 MW in their paper; however, these were calculated incorrectly and the revised ERP is consistent with the way they are calculated for the present paper using the original heater logs for their data set. Their result estimates the ERP to be higher than our electric field estimates predict; however, the D region absorption in the two experiments may have been considerably different.

[53] In Figure 9, we show the maximum power measured for the last 5 s UHF ion-line spectrum shoulders for O- and X-mode (O-mode leakage) in red and black, respectively. We note that the ion-line enhancements for the X-mode pulses are not present until after 11:00 UT. Before then, the height at which power is measured is the height at which it first appears at 11:00 UT (i.e., ∼210 km).

[54] The steady state O-mode backscattered signal is lower in power than for most of the X-mode cases, even though the O-mode ERP was much higher than the O-mode leakage in the X-mode pulse on the ground. This indicates that between the ground and the matching height, the O-mode pump pulse power is reduced to levels below that

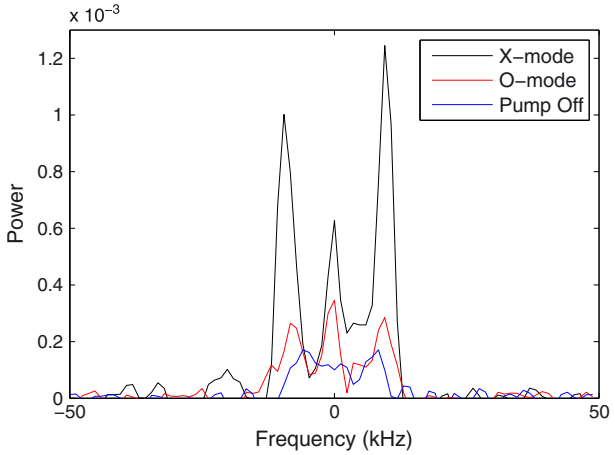

Figure 8. Example UHF ion-line spectra for O- and X-mode in red and black, respectively. The blue spectrum is a typical case for when the heater is off.

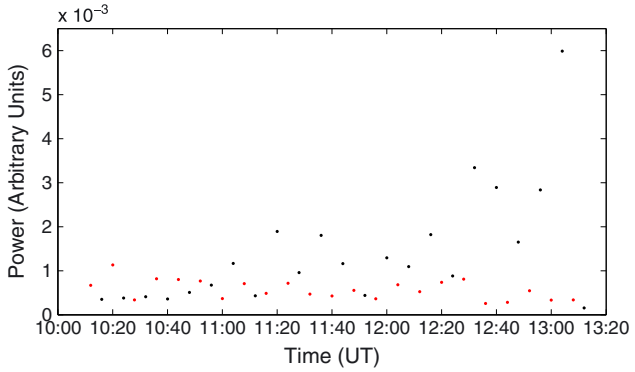

Figure 9. The maximum power of the UHF ion-line spectra shoulders shown at the ion-line enhancement range gate during the last 5 s of pump on. The red/black dots show the maximum power for O/X-modes, respectively.

of the O-mode leakage power found in the X-mode pump pulse. We assume that the power density decreases significantly because of the presence of striations causing anomalous absorption and possibly because of beam divergence due to refraction caused by the ionization. As time progresses the maximum O-mode backscattered power remains relatively constant despite the decreasing absorption. This probably means that the striations permit a constant flux of heater power to stimulate PDI/OTSI, i.e., they regulate the amount of pump power that can pass through. For the X-mode (O-mode leakage) cases where striations are not present, or are very weak, the spectral power increases with increasing heater power flux (see Figure 1b).

[55] We modeled the effect of the ionization on the beam divergence and refraction of the pump wave during heating using the *Jones and Stephenson* [1975] ray tracing model. We estimate a simple Gaussian enhancement in electron density close to reflection height, which causes the reflection height to decrease in altitude by an amount consistent with that of the observed descending ion lines. We estimate that, in the center of the beam, the heater power flux can decrease to 60% of its original amount. *Bryers et al.* [2012] found that, without the additional beam divergence which may be present due to ionization, around 25% of the power flux may be lost due to refraction. This would have the effect of increasing the O-mode efficiency calculation discussed in section 4.1 by a factor of ∼1.7.

5. Conclusion

[56] We have compared the electron heating effects from O- and X-mode ionospheric pumping experiments. We have quantified the effect which O-mode resonant heating mechanisms have on the height-integrated electron heating rate and the electron temperature enhancements compared to a nonresonant X-mode pump wave.

[57] The height-integrated electron heating rate for X-mode pumping was quantified using two independent methods. The first was done by applying a Gaussian heat source and estimating the electron temperature height profile until it matched the observed profile. The second method was done by estimating the electric field strength of the pump wave as it propagated through the ionosphere. Both methods estimate the height-integrated electron heating rate with good agreement for X-mode pumping. For O-mode pumping, the electric field model can only estimate the nonresonant heating whereas the temperature profile fitting method calculates the total height-integrated heat source. From the difference, we found the height-integrated heating rate due to wave plasma resonance and found it to be approximately 2–5 times that of the nonresonant component, assuming zero anomalous absorption of the nonresonant component. In reality, less energy is available at reflection, to heat the electrons via the nonresonant mechanism, since pump energy is being lost at the UHR height due to the presence of striations.

[58] We find the signature for O-mode pump-induced ion-line enhancements during the X-mode pumping cycles and attribute this to a small leakage of O-mode power. During O-mode pumping, we observed a decrease in the ion-line enhancement altitude and show that ionization of the neutral components in the ionosphere as the most likely cause. By inferring an electron flux needed to observe the measured rate of ionization, we estimate that in total, 10–20% of the pump wave power is transferred to high energy suprathermal electrons.

Appendix A: Testing the Electric Field Model

[59] To test the electric field model discussed in section 2.2 for O-mode pumping, we used a data set from 11 November 2001. The experiment performed was field-aligned pumping, 2 min on, 2 min off, with 3 ERP levels (121, 243, and 523 MW), on the fourth gyroharmonic frequency (5.423 MHz in the *F* region). When pumping on a gyroharmonic frequency, UHR and the growth of striations is suppressed allowing a comparison of the two methods for determining the height-integrated heating rate. When UHR cannot be stimulated, nonresonant heating becomes responsible for the electron temperature enhancement, assuming weak heating from Langmuir turbulence. Figure A1 shows the nonresonant height-integrated heating estimate from the electric field model, $J_{\text{nonresonant}}$, and J_{total} from the heat source

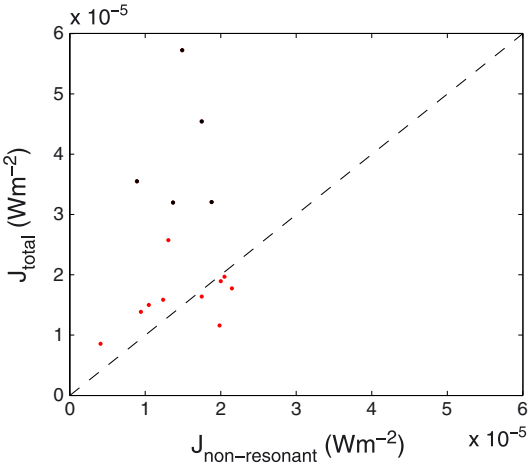

Figure A1. Data from 11 November 2001 showing the height-integrated heating rate determined via the two independent methods. The black dots show where $|\Delta f| = |4f_e - f_o| > 100$ kHz at the UHR height.

fitting method. The dashed line shows where $J_{\text{nonresonant}} = J_{\text{total}}$. The two methods agree well (red dots) indicating that nonresonant heating constitutes the main heat source here, and the absence of resonances allows the electric field model to accurately determine the total height-integrated heating rate. We note that some outliers exist (black dots), which are heating pulses occurring toward the end of the experiment as the ionosphere becomes closer to being underdense. Here $|\Delta f| = |4f_e - f_o| > 100$ kHz at the UHR height, i.e., the pump frequency is no longer sufficiently close to the gyroharmonic and UHR can be established giving an additional heat source.

[60] *Gustavsson et al.* [2006] performed a heating experiment with a sweeping pump frequency through the fourth gyroharmonic at EISCAT. They found an asymmetry whereby artificial optical intensities were brighter when pumping above the gyroharmonic ($\Delta f \sim 75$ kHz). This implies that UHR had established itself when Δf was sufficiently large. This agrees well with our results which shows the same trend and explains why the outliers exist in Figure A1.

[61] We can therefore conclude that the electric field model is good for 12° off-vertical (field-aligned) cases at EISCAT for both O- and X-mode pumping.

[62] **Acknowledgments.** EISCAT is an international scientific association supported by research organizations in China (CRIRP), Finland (SA), Japan (NIPR and STEL), Norway (NFR), Sweden (VR), and the United Kingdom (NERC). The authors would like to thank B. Gustavsson for providing us with the cross sections used in this work.

[63] Robert Lysak thanks Savely Grach and Terence Ronald Robinson for their assistance in evaluating this paper.

References

Ashrafi, M., M. Kosch, and F. Honary (2006), Heater-induced altitude descent of the EISCAT UHF ion-line enhancements: Observations and modeling, *Adv. Space Res.*, *38*, 2645.

Banks, P. M. (1966), Charged particle temperatures and electron thermal conductivity in the upper atmosphere, *Ann. Geophys.*, *22*, 577–587.

Blagoveshchenskaya, N. F., H. C. Carlson Jr., V. A. Kornienko, T. D. Borisova, M. T. Rietveld, T. K. Yeoman, and A. Brekke (2009), Phenomena induced by powerful HF pumping towards magnetic zenith with a frequency near the F-region critical frequency and the third electron gyro harmonic frequency, *Ann. Geophys.*, *27*, 131–145.

Bryers, C. J., M. J. Kosch, A. Senior, M. T. Rietveld, and T. K. Yeoman (2012), EISCAT observations of pump-enhanced plasma temperature and optical emission excitation rate as a function of power flux, *J. Geophys. Res.*, *117*, A09301, doi:10.1029/2012JA017897.

Campbell, L., M. J. Brunger, D. C. Cartwright, and P. J. O. Teubner (2004), Production of vibrationally excited N_2 by electron impact, *Planet. Space Sci.*, *52*, 815–822.

Djuth, F. T., P. Stubbe, M. P. Sulzer, H. Kohl, M. T. Rietveld, and J. H. Elder (1994), Altitude characteristics of plasma turbulence excited with the Tromsø Superheater, *Rev. J. Geophys. Res.*, *99*, 333–339, doi:10.1029/93JA02289.

Fejer, J. A. (1979), Ionospheric modification and parametric instabilities, *Rev. Geophys.*, *17*, 135–153, doi:10.1029/RG017i001p00135.

Graham, K. N., and J. A. Fejer (1976), Anomalous radio wave absorption due to ionospheric heating effects, *Radio Sci.*, *11*, 1057–1063, doi:10.1029/RS011i012p01057.

Gustavsson, B., et al. (2006), The electron energy distribution during HF pumping, a picture painted with all colors, *Ann. Geophys.*, *23*, 1747–1754, doi:10.5194/angeo-23-1747-2005.

Gustavsson, B., T. B. Leyser, M. Kosch, M. T. Rietveld, Å. Steen, B. U. E. Brändström, and T. B. Aso (2006), Electron gyroharmonic effects in ionization and electron acceleration during HF pumping in the ionosphere, *Phys. Rev. Lett.*, *97*, 195,002, doi:10.1103/PhysRevLett.97.195002.

Gustavsson, B., and B. Eliasson (2008), HF radio wave acceleration of ionospheric electrons: Analysis of HF-induced optical enhancements, *J. Geophys. Res.*, *113*, A08319, doi:10.1029/2007JA012,913.

Gustavsson, B., M. T. Rietveld, N. V. Ivchenko, and M. J. Kosch (2010), Rise and fall of electron temperatures: Ohmic heating of ionospheric electrons from underdense HF radio wave pumping, *J. Geophys. Res.*, *115*, A12332, doi:10.1029/2010JA015873.

Hansen, J. D., G. J. Morales, and J. E. Maggs (1992), Large-scale HF-induced ionospheric modifications: Theory and modeling, *J. Geophys. Res.*, *97*(A11), 17,019–17,032.

Itikawa, Y., M. Hayashi, A. Ichimura, K. Onda, K. Sakimoto, K. Takayanagi, M. Nakamura, H. Nishimura, and T. Takayanagi (1986), Cross sections for collisions of electrons and photons with nitrogen molecules, *J. Phys. Chem. Ref. Data*, *15*, 985–1010.

Itikawa, Y., A. Ichimura, K. Onda, K. Sakimoto, K. Takayanagi, Y. Hatano, M. Hayashi, H. Nishimura, and S. Tsurubuchi (1989), Cross sections for collisions of electrons and photons with oxygen molecules, *J. Phys. Chem. Ref. Data*, *18*, 23–42.

Itikawa, Y., and A. Ichimura (1990), Cross sections for collisions of electrons and photons with atomic oxygen, *J. Phys. Chem. Ref. Data*, *19*, 637–651.

Jones, D. B., L. Campbell, M. J. Bottema, and M. J. Brunger (2003), New electron energy transfer rates for vibrational excitation of O_2, *New J. Phys.*, *5*(1), 114.

Jones, R. M., and J. J. Stephenson, (1975), A versatile three-dimensional ray tracing computer program, *Office of Telecommunications Report 75–76*, US Government Printing Office, Washington, D. C.

Kosch, M. J., T. Pedersen, M. T. Rietveld, B. Gustavsson, S. M. Grach, and T. Hagfors (2007), Artificial optical emissions in the high-latitude thermosphere induced by powerful radio waves: An observational review, *Adv. in Space Res.*, *40*, 365–376.

Meltz, G., and R. E. LeLevier (1970), Heating the F region by deviative absorption of radio waves, *J. Geophys. Res.*, *75*(31), 6406–6416, doi:10.1029/JA075i031p06406.

Pavlov, A. V. (1998a), New electron energy transfer rates for vibrational excitation of N_2, *Ann. Geophys.*, *16*, 176–182

Pavlov, A. V. (1998b), New electron energy transfer and cooling rates by excitation of O_2, *Ann. Geophys.*, *16*, 1007–1013.

Pedersen, T., B. Gustavsson, E. Mishin, E. MacKenzie, H. C. Carlson, M. Starks, and T. Mills (2009), Optical ring formation and ionization production in high-power HF heating experiments at HAARP, *Geophys. Res. Lett.*, *36*, L18107, doi:10.1029/2009GL040047.

Pedersen, T., M. McCarrick, B. Reinisch, B. Watkins, and R. Hamel (2011), Production of artifcial ionospheric layers by frequency sweeping near the 2nd gyroharmonic, *Ann. Geophys.*, *29*, 47–51.

Richards, P. G. (2011), Reexamination of ionospheric photochemistry, *J. Geophys. Res.*, *116*, A08307, doi:10.1029/2011JA016613.

Rietveld, M. T., H. Kohl, H. Kopka, and P. Stubbe (1993), Introduction to ionospheric heating at Troms—I. Experimental overview, *J. Atmos. Sol. Terr. Phys.*, *55*, 577–599.

Rietveld, M. T., B. Isham, H. Kohl, C. La Hoz, and T. Hagfors (2000), Measurements of HF-enhanced plasma and ion-lines at EISCAT with high-altitude resolution, *J. Geophys. Res.*, *105*, 7429–7439, doi:10.1029/1999JA900476.

Rishbeth, H., and A. P. van Eyken (1993), EISCAT: Early history and the first ten years of operation, *J. Atmos. Terr. Phys.*, *55*, 525–542.

Robinson, T. R. (1988), The excitation of plasma waves and irregularities in the ionosphere by means of high power radio waves, *Plasma Phys. Control. Fusion.*, *30*, 45–56, doi:10.1088/0741-3335/30/1/006.

Robinson, T. R. (1989), The heating of the high latitude ionosphere by high power radio waves, *Phys. Rep.*, *179*, 79–209.

Schunk, R. W., and A. F. Nagy (1978), Electron temperatures in the F region of the ionosphere: Theory and observations, *Rev. Geophys.*, *16*(3), 355–399.

Schunk, R. W., and A. F. Nagy (2000), *Ionospheric Physics, Plasma Physics, and Chemistry*, Cambridge Univ. Press, Cambridge, U. K.

Senior, A., M. T. Rietveld, N. D. Borisov, M. J. Kosch, T. K. Yeoman, and F. Honary (2004), Multi-frequency HF radar measurements of artificial F-region field-aligned irregularities, *Ann. Geo.*, *22*, 3503–3511.

Senior, A., M. T. Rietveld, M. J. Kosch, and W. Singer (2010), Diagnosing radio plasma heating in the polar summer mesosphere using cross-modulation: Theory and observations, *J. Geophys. Res.*, *A09*, 318, doi:10.1029/2010JA015379.

Shoucri, M. M., G. J. Morales, and J. E. Maggs (1984), Ohmic heating of the polar F-region by HF pulses, *J. Geophys. Res*, *89*, 2907–2917.

Singer, W., R. Latteck, and D. A. Holdsworth (2008), A new narrow beam Doppler radar at 3 MHz for studies of the high latitude middle atmosphere, *Adv. Space Res.*, *41*, 1488–1494, doi:10.1016/j.asr.2007.10.006.

Stubbe, P., H. Kohl, and M. T. Rietveld (1992), Langmuir turbulence and ionospheric modification, *J. Geophys. Res.*, *97*, 6285–6297, doi:10.1029/91JA03047.

Wang, J. G., D. L. Newman, and M. V. Goldman (1997), Vlasov simulation of electron heating by Langmuir turbulence near the critical altitude in the radiation-modified ionosphere, *J. Atmos. Solar and Terr. Phys.*, *59*, 2461–2474.